

Contents list available at CBIORE journal website

# 

Journal homepage: https://ijred.cbiore.id



**Research Article** 

# Frequency control enhancement for hybrid microgrid using multiterminal multi-function inverter

Doaa Eida\* Doaa Eida Elmasry Adel El Samahy, Farag Elnagahy, Erhab Youssef Doaa Eida Elnagahy, Erhab Youssef Doaa Elnagahy, Erhab Elna

- <sup>a</sup> National Research Institute of Astronomy and Geophysics (NRIAG), Astronomy Department, Cairo, 11421, Egypt
- <sup>b</sup> Faculty of Engineering, Helwan University, Department of Electrical Power and Machines Engineering, Cairo, 11792, Egypt
- <sup>c</sup> College of Engineering, Prince Sattam Bin Abdulaziz University, Department of Electrical Engineering, Al-Kharj, 11942, Saudi Arabia

**Abstract**. Renewable energy sources (RESs) are considered a crucial energy transformation to reduce carbon emissions, so more RESs are being integrated into contemporary power systems. Power electronic converters are extensively utilized to connect power grids with renewable generators to manage the fluctuations and unpredictability of these renewable energy sources. This paper introduces a multi-terminal multi-function inverter (MT-MF) designed for a battery energy storage system (BESS) to maintain the frequency stability of a hybrid microgrid (MG). The MG comprises a photovoltaic generation system, a diesel generator, BESS, and two loads: one constant load and the other variable, fed through a medium-voltage radial feeding system. An introduced approach involves utilizing a model predictive control controlled virtual synchronous generator (MPC-VSG) for BESS. This method offers inertia support during transient states and improves the dynamic characteristics of system frequency. In addition, it enables the connection of multiple batteries, provides individualized control for each, and supports the injection of reactive power into the MG. The required power from the BESS is shared between the two batteries using the low pass filter technique. The simulation outcomes affirm the proposed control strategy's effectiveness and underscore the MT-MF inverter approach's potential in integrating extensive RESs. This paper also explores how the proposed technique outperforms other methods in improving frequency stability.

**Keywords:** Frequency Stability, Microgrids, Photovoltaic generation, renewable energy, Virtual Synchronous Generator, storage Battery, Grid Integration, nonlinear controller.



@ The author(s). Published by CBIORE. This is an open access article under the CC BY-SA license (http://creativecommons.org/licenses/by-sa/4.0/).

Received: 26<sup>th</sup> Feb 2024; Revised: 17<sup>th</sup> April 2024; Accepted: 12<sup>th</sup> May 2024; Available online: 15<sup>th</sup> May 2024

#### 1. Introduction

Microgrids (MGs) have appeared as an economical option for combining renewable energy sources (RESs) into power systems (Zhong *et al.*, 2022). These MGs comprise distributed generator resources (DGRs), such as solar panels, wind turbines, energy storage devices (e.g., batteries), and generators, which generate the required power. The generated power can be transferred into the utility grid or directly supplied to the connected loads within the MG (Khooban *et al.*, 2017; Stadler and Naslé 2019).

MG stability is defined as the capability to maintain in operation during disturbances. The concept of stability within MGs can be categorized into two primary aspects: one involving the control systems of the equipment and the other involving the distribution and equilibrium of active and reactive power. It is important to note that instability in MG, whether in the equipment control or power sharing, can manifest as either short-term or long-term issues; short-term stability concerns typically occur within a few seconds, while long-term stability concerns extend beyond this time frame, affecting the overall system (Farrokhabadi *et al.*, 2020).

Large-signal analysis, also known as transient stability analysis, is centered on major disturbances like ground faults, abrupt power losses, transitions to off-grid operation, and similar events. These frequent disruptions can significantly affect the system's stable operation, potentially leading to system breakdown. Hence, they demand increased attention. Substantial disturbances can lead to significant deviations in frequency, voltage, and power swings among various DERs (Farrokhabadi *et al.*, 2020).

Frequency stability is a subcategory of transient stability, where it is a notable challenge in MGs due to systemic characteristics such as low system inertia and an extensive presence of alternating RESs. The sensitivity to significant disturbances is impaired in MGs because of the restricted number of generation units, elevating the probability of notable disturbances during generator outages. Consequently, among such disturbances, the system frequency may experience substantial deviations quickly, threatening the system's overall stability (Borghetti *et al.*, 2010; Farrokhabadi *et al.*, 2020; Delille *et al.*, 2012).

Distributed inverters become the principal components in MGs for injecting energy produced by RESs into the power system. Accordingly, the increasing reliance on inverters has

Corresponding author Email: doaa\_eid@nriag.sci.eg (D. Eid)

significantly reduced the overall inertia of MG (Ghodsi *et al.*, 2022). Reduction in the amount of mechanical inertia of the MG primes to more pronounced frequency responses to disturbances and faults. It causes severe stability problems in the MG compared with the conventional power system characterized by synchronous generators (SGs) (Huang *et al.*, 2017); (Kerdphol *et al.*, 2021).

The converter connected to the MG from the RES can be managed to enhance frequency dynamics. This goal is accomplished by mimicking the governor control seen in traditional power stations, known as droop control. It involves simulating the inertial response of a rotating machine, called virtual inertia control (VIC), or replicating the swing equation of a synchronous generator, termed virtual synchronous generator (VSG) (Cheng et al., 2020); (Shuai et al., 2019). In contrast to SGs, VSGs can manage active and reactive power outputs using control loops. During a transient period, such as a grounded fault, the inverter's output reactive power experiences a sudden surge. This surge triggers an abrupt reduction in the inverter's internal voltage amplitude due to the operation of the reactive power control loop (Cheng et al., 2020; Shuai et al., 2019). Numerous VSG schemes have been suggested and categorized into current-controlled or voltagecontrolled VSGs. The initial proposal (Beck and Hesse 2007); (Rodriguez et al., 2018) introduces a current-controlled VSG scheme, but it exclusively utilizes a current control loop, limiting its operation to connected grids. In (Liu et al., 2016); (Zhong and Weiss 2011), an alternative voltage-controlled VSG scheme is presented, enabling operation in islanded mode.

There are two ways for VSG technology to support the system frequency by controlling the output power of the inverter and the DGs: those with an energy storage system (ESS) (Hirase et al., 2018) and those without an ESS (Rosewater et al., 2019). Controlling without ESS may require an accumulated quantity of energy or power reserve. The inertia and damping parameters of the electric generator within the wind generation system are employed as a reserve power source to assist in maintaining the frequency of the MG (Pratap et al., 2015); (Yousef et al., 2021). However, the PV system does not have inertia or damping parameters. The de-loading technique, where the PV runs under its maximum power (MP), is an alternate method of providing frequency support (Eid et al., 2022). Integrating an ideal ESS into a PV-based power system in which the power reserve is sourced from the ESS's stored energy in ESS (Zhang et al., 2020); (Ur Rehman et al., 2021).

Multi-terminal multi-function (MT-MF) inverter is suggested as a power electronic device to reduce the number of passive components and conversion stages between batteries and the MG (Youssef *et al.*, 2019). The MT-MF inverter is adaptable and can perform various functions, including power factor correction, voltage regulation, and harmonic mitigation. It can also operate as a VSG to enhance frequency stability. The converter operates using a matrix of semiconductor switches to control the power flow between the input and output sides.

Recent research on model predictive control (MPC) in ESS has primarily concentrated on coordinating charging and discharging across multiple ESSs using the MPC methodology (Garcia-Torres *et al.*, 2019); (Bo and Johansen 2017). Furthermore, the MPC controller can determine the current power reference by forecasting the necessary output power for the upcoming sampling period, enhancing power tracking performance (Giuseppi *et al.*, 2019). Most literature on VSG employs the pulse width modulation (PWM) technique to

transmit signals to the grid-tied converter. In contrast, MPC generates switching signals internally, eliminating the need for external PWM generators. The main contributions of this study are summarized as follows:

- Designing of MT-MF inverter to interface two batteries, enabling individual, active power management for both batteries.
- Designing VSG-based BESS and determining the VSG control parameters Droop factor, Moment of inertia, damping coefficient, and Droop constant using trial and error method.
- The design of MPC-VSG control involves calculating the required increase in power by solving the optimized cost function squared errors. This is done to improve the frequency response during various disturbances.
- Investigating the MG's performance using MPC-VSG with squared errors for active and reactive powers objective function under severe disturbance.

This paper is structured into six sections: Firstly, section introduces a brief introduction, including the problem definition, motivation, and a literature review. Then, the proposed microgrid modeling is derived in section. The section discusses the proposed MPC-VSG-based BESS control

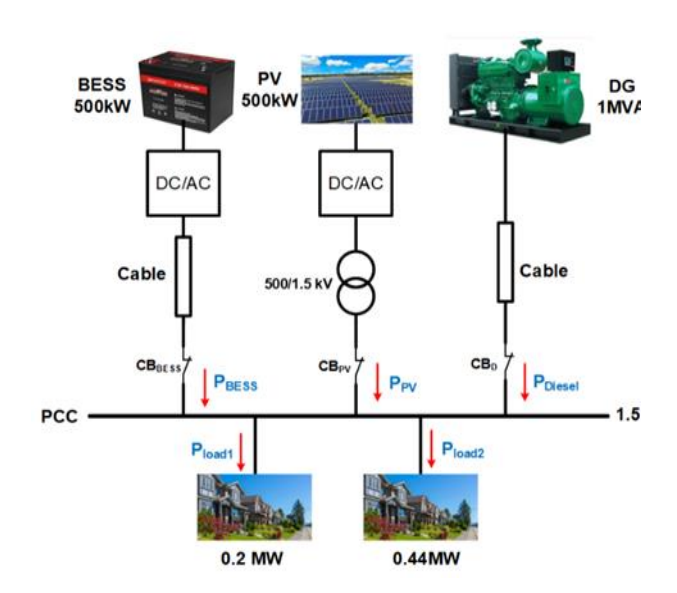


Fig. 1. Microgrid under study.

**Table 1**Microgrid capacity and configuration

Parameter	Symbol	Value
PV rated power [MW]	$P_{ m pv}$	0.5
DU rated power [MW]	$P_{ m diesel}$	1
BESS rated power [MW]	$P_{\mathrm{BATT}}$	0.3
PL rated power [MW]	$P_{ m L}$	0.64
MG phase rms voltage [KV]	V	1.5
Sampling time $[\mu_S]$	$T_{\mathrm{s}}$	20
MG frequency [Hz]	$F_{ m g}$	50

concept, and section discusses the simulation results. Finally, the conclusions are summarized in section.

## 2. Proposed Microgrid Modelling

A small-scale MG that is disconnected from the main network includes a conventional diesel engine generator (DEG), solar photovoltaic PV system that is linked to MG through a voltage source converter, and battery energy storage systems (BESS) that interfaced with MG using MT-MF inverter, which is connected to loads. Figure 1 shows the system under study. These converters regulate the injected power from these resources to the point of common coupling (PCC). The system configuration includes a 1 MW DEG and a 0.5 MW PV generator supplying residential and industrial loads with 0.2 MW and 0.44 MW, respectively. A BESS is also integrated to enhance the MG's stability. The MG capacity and parameters are listed in Table 1.

#### 2.1. PV generation system

PV is equipped with a Maximum Power Point Tracking (MPPT) controller, enabling it to extract the maximum available power as solar radiance fluctuates. Specific details about the MPPT algorithm for the PV system can be referenced (Oulcaid  $et\ al.$ , 2016). The mathematical model that expresses the PV system is constructed as in (Hassanzadeh  $et\ al.$ , 2020). The power output of a PV system is contingent on the solar radiation (G) and ambient temperature ( $T_{amb}$ ). The PV's output power experiences a linear rise with increasing solar radiation, while it declines with elevated ambient temperatures. Consequently, these factors influence the instantaneous output power of a PV array, as outlined in (Kazem  $et\ al.$ , 2017).

$$P_{pv} = \left(P_{pv,STC} \frac{G}{G_{STC}} \left[ -\gamma \left( T_j - T_{STC} \right) \right] \right) N_{pvs} N_{pvp,} \qquad (1)$$

$$T_j = T_{amb} + T_{STC} \frac{G}{800}.$$

Here in Equation (1),  $P_{pv,STC}$  denotes the rated power of the PV,  $G_{STC}$  and  $T_{STC}$  represent the standard test conditions for solar radiation and cell temperature, respectively, and  $\gamma$  is the temperature coefficient of the PV module power, which can be extracted from the datasheet (Patel and Beik 2021).  $T_j$  is the cell temperature, and  $N_{pvs}$ ,  $N_{pvp}$ , represents the number of modules in series and in parallel that compose the generator.

#### 2.2. Diesel generation unit

Diesel generators find extensive use in hybrid microgrid systems. Figure 2 illustrates the block diagram for the simplified diesel generator and governor models. The model parameters are listed in Table 2.

The fundamental parts of DU are the engine, governor, excitation, and synchronous generator. A governor is a mechanical or electromechanical device that uses the fuel intake to adjust an engine's speed automatically. The turbine is kept operating at its intended speed by the controller for the engine, which is a straightforward speed governor. The speed governor's output is a throttle signal, which controls how much gasoline is injected into the engine (Benhamed *et al.*, 2016).

**Table 2**Diesel Generator Model Parameters.

Symbol	Description	Units
m	Speed droop gain	Unitless
$w^*$	Speed reference	p.u.
$P^*$	Power reference	p.u.
$T_1: T_6$	Diesel engine time constants	sec
$T_E$	AVR gain	sec

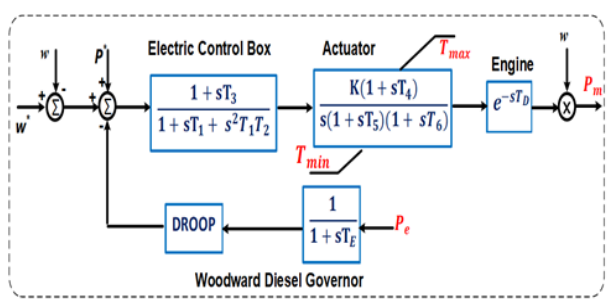


Fig. 2. Diesel generator model.

#### 2.3. Proposed system

The suggested system consists of a multi-terminal inverter (3x3); its DC side terminals connect two Lithium-Ion batteries, and the AC side connects to the MG as depicted in Figure 3, whereas the batteries linked to the MT inverter through a DC inductor  $L_{dc}$  with small parasitic resistance  $r_{dc}$ . Moreover, the AC side of that inverter is linked to the MG bus via a second-order filter ( $C_f$ ,  $L_f$ ,  $R_f$ ). The paramet1er specifications for the proposed model are listed in Table 3.

## 2.3.1. Battery model

Table 3

The dynamic simulation of the Lithium-Ion battery's modeling involves applying the discharging and charging equations presented in (Tremblay and Dessaint 2009).

System and control parameters

Parameter	Symbol	Value
MG filter inductance [mH]	$L_{\mathrm{f}}$	4
MG damping resistance $[\Omega]$	$R_{ m f}$	33
MG filter capacitance delta [F]	$C_{ m f}$	6
DC link inductance [mH]	$L_{ m dc}$	12.5
DC link resistance $[\Omega]$	$r_{ m dc}$	0.1
Droop factor Moment of inertia [kg. m2] Damping coefficient [pu]	K <sub>d</sub> J D	0.0001 167 0.00005
Reactive power droop constant [pu] Weights of BESS active power for VSG [pu] Weights of MG reactive active power for VSG [pu]	$K_{ m v}$ $J_1$ $J_2$	20 150 50

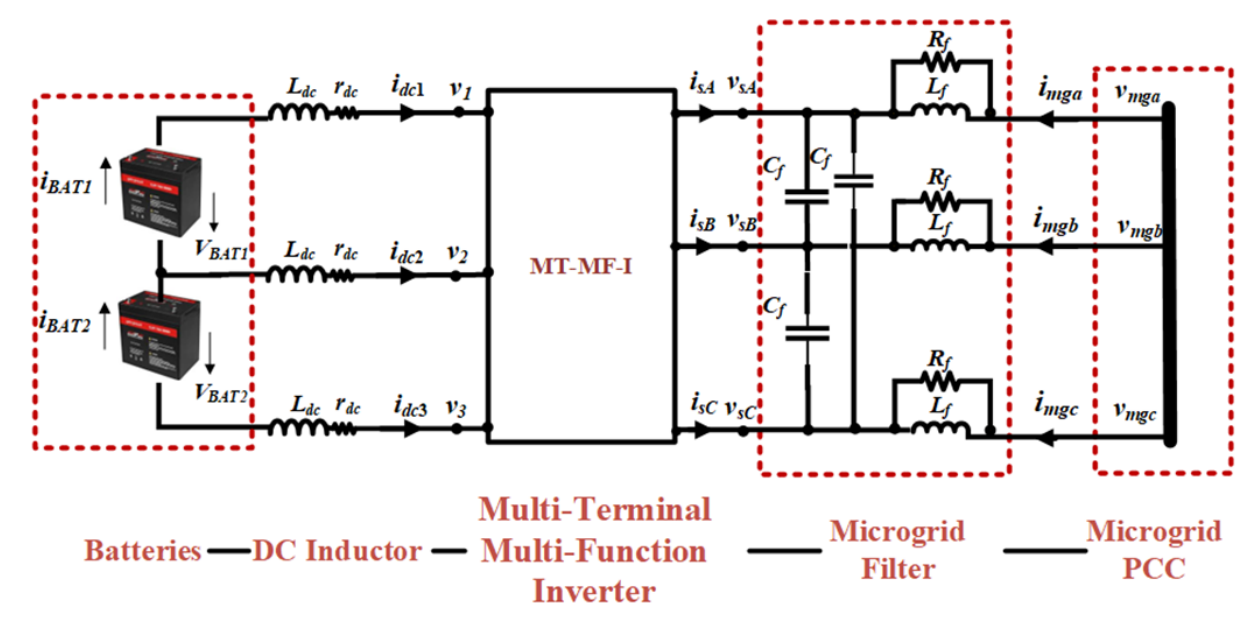


Fig. 3. Proposed BESS Model.

$$\begin{aligned} Discharge: V_{BAT} &= E_0 - R.\,i - K\frac{Q}{Q-it}.(it+i^*) \\ &\quad + A\exp(-B.it), \end{aligned}$$
 
$$Charge: V_{BAT} &= E_0 - R.\,i - K\frac{Q}{it-0.1-Q}.i^* - K\frac{Q}{Q-it}.it \\ &\quad + A\exp(-B.it). \end{aligned}$$

In the given Equation (2),  $V_{BAT}$  and  $E_0$  denotes battery voltage (V) and battery constant voltage (V), respectively. While K and Q represent polarisation constant (V/(Ah)) or polarization as in (Sikder and Pal 2020), resistance ( $\Omega$ ) and battery capacity (Ah), it corresponds to  $\int i \ dt$  signifies the actual battery charge (Ah), A represents the amplitude of the exponential zone (V), B represents the inverse of the time constant ( $Ah^{-1}$ ), R denotes the internal resistance in ohms ( $\Omega$ ), i represents the battery current in (A), and  $i^*$  represents the filtered current in (A).

## 2.3.2. MT-MF inverter model-based BESS

To create a model for a three-terminal inverter, ideal bidirectional switches  $(S_{ja}, S_{jb}, S_{jc})$ , in which 'j' denotes the terminal number (1,2,3) are employed. The switches establish connections between the batteries and the AC side of the MG. At any given moment, only one of the three switches per terminal should be in the closed position. Each switch is assigned a value of 1 at the closed state and 0 at the open state, as indicated in literature (Rodriguez 2019). Equation (3) is derived to give the switches the states:

$$S = \begin{bmatrix} S_{1a} & S_{1b} & S_{1c} \\ S_{2a} & S_{2b} & S_{2c} \\ S_{3a} & S_{3b} & S_{3c} \end{bmatrix}, \quad S_{1a} + S_{1b} + S_{1c} = 1.$$
 (3)

Utilizing Equation (3), the DC link voltages ( $v_1$ ,  $v_2$ ,  $v_3$ ), which are the inverter voltages on the DC side, can be derived from the phase voltages ( $v_{SA}$ ,  $v_{SB}$ ,  $v_{SC}$ ) on the AC side of the inverter. Similarly, the AC currents of the matrix inverter,

represented as  $i_{sA}$ ,  $i_{sB}$ ,  $i_{sC}$ , can be computed from the current on the DC side of the inverter, as articulated in Equation (4):

$$\begin{bmatrix} v_1 \\ v_2 \\ v_3 \end{bmatrix} = S \begin{bmatrix} v_{SA} \\ v_{SB} \\ v_{SC} \end{bmatrix}, \begin{bmatrix} i_{SA} \\ i_{SB} \\ i_{SC} \end{bmatrix} = S^T \begin{bmatrix} i_{dc1} \\ i_{dc2} \\ i_{dc3} \end{bmatrix}. \tag{4}$$

#### 2.3.3. MT-MF inverter DC side model

Due to the above constraints in Equation (3), 27 permissible switching combinations exist. The connection of batteries to the inverter is established using a DC inductor. The current dynamics of the batteries are derived from Equation (5).

$$\frac{di_{BAT1}}{dt} = -\frac{r_d}{L_d} i_{BAT1} - \frac{v_{12} + 2v_{23}}{3L_d} + \frac{V_{BAT1} + 2V_{BAT2}}{3L_d}.$$

$$\frac{di_{BAT2}}{dt} = -\frac{r_d}{L_d} i_{BAT2} - \frac{v_{12} + 2v_{23}}{3L_d} + \frac{V_{BAT1} + 2V_{BAT2}}{3L_d}.$$
(5)

Where ( $V_{BAT1}$ ,  $V_{BAT2}$ ,  $i_{BAT1}$ ,  $i_{BAT2}$ ) are the voltages and currents for batteries. Consequently, the power of each battery system is computed based on Equation (6):

$$P_{BAT1} = i_{BAT1}V_{BAT1},$$

$$P_{BAT2} = i_{BAT2} V_{BAT2}, \tag{6}$$

## 2.3.4. Modelling on the MT-MF inverter AC grid side

The system depicted in Figure 3, using Kirchhoff's law, considering the transmission of power from the AC side to the DC side, one can derive the state-space model of the AC side of the MT-MF-inverter.

The MG currents ( $i_{mga}$ ,  $i_{mgb}$ ,  $i_{mgc}$ ) are derived from Equation (7) and are contingent upon. The currents flowing through the inductors ( $i_{la}$ ,  $i_{lb}$ ,  $i_{lc}$ ), the inductance of the filter ( $L_f$ ), and the resistance for damping ( $R_f$ ).

$$\begin{bmatrix} i_{mga} \\ i_{mgb} \\ i_{mgc} \end{bmatrix} = \begin{bmatrix} i_{la} \\ i_{lb} \\ i_{lc} \end{bmatrix} + \begin{bmatrix} \frac{L_f}{R_f} & 0 & 0 \\ 0 & \frac{L_f}{R_f} & 0 \\ 0 & 0 & \frac{L_f}{R_f} \end{bmatrix} \begin{bmatrix} \frac{di_{la}}{dt} \\ \frac{di_{lb}}{dt} \\ \frac{di_{lc}}{dt} \end{bmatrix}$$
(7)

Equation (8) represent the capacitor's voltages dynamics:

$$\begin{bmatrix}
\frac{dv_{sab}}{dt} \\
\frac{dv_{sbc}}{dt} \\
\frac{dv_{sca}}{dt}
\end{bmatrix} = \begin{bmatrix}
0 & -\frac{2}{3*C_f} & -\frac{1}{3C_f} \\
-\frac{1}{3C_f} & 0 & -\frac{2}{3C_f} \\
-\frac{2}{3C_f} & -\frac{1}{3C_f} & 0
\end{bmatrix} \begin{bmatrix}
i_{mga} \\
i_{mgb} \\
i_{mgc}
\end{bmatrix} \\
+ \begin{bmatrix}
0 & \frac{2}{3C_f} & \frac{1}{3C_f} \\
\frac{1}{3C_f} & 0 & \frac{2}{3C_f} \\
\frac{2}{3C_f} & \frac{1}{3C_f} & 0
\end{bmatrix} \begin{bmatrix}
i_{sa} \\
i_{sb} \\
i_{sc}
\end{bmatrix}$$
(8)

By utilizing Equation (7), the dynamics of the inductor currents can be expressed as in Equation (9):

$$\begin{bmatrix}
\frac{di_{la}}{dt} \\
\frac{di_{lb}}{dt} \\
\frac{di_{lc}}{dt}
\end{bmatrix} = \begin{bmatrix}
-\frac{2}{3*L_f} & -\frac{1}{3L_f} & 0 \\
0 & -\frac{2}{3L_f} & -\frac{1}{3L_f} \\
-\frac{1}{3L_f} & 0 & -\frac{2}{3L_f}
\end{bmatrix} \begin{bmatrix} v_{sab} \\ v_{sbc} \\ v_{sca} \end{bmatrix} + \begin{bmatrix} \frac{1}{L_f} & 0 & 0 \\ 0 & \frac{1}{L_f} & 0 \\ 0 & 0 & \frac{1}{L_f} \end{bmatrix} \begin{bmatrix} v_{mga} \\ v_{mgb} \\ v_{mgc} \end{bmatrix} \tag{9}$$

To ensure independent control actions for the BESS power and reactive power, the dynamic equations of the MG side (including MG currents, inductor currents, and capacitor voltages) will undergo conversion to the dq frame using the Concordia transformation (abc to  $\alpha\beta$  coordinates) as outlined in Equation (10) and subsequently applying the Park transformation ( $\alpha\beta$  B to dq coordinates). This conversion reduces three-dimensional computations into two dimensions, demanding less computational power and enhancing efficiency. The load model employed in this study encompasses linear loads.

To derive the state-space model Equations (7), (8), (9) in  $\alpha\beta$  coordinates, the Concordia transformation Equation (10) is employed. This transformation involves converting the variables  $X_{abc}$  to  $X_{\alpha\beta}$ , as defined by:  $X_{\alpha\beta} = C^T X_{abc}$ .

$$C = \sqrt{\frac{2}{3}} \begin{bmatrix} -\frac{1}{2} & \frac{\sqrt{3}}{2} & \frac{1}{\sqrt{2}} \\ -\frac{1}{2} & -\frac{\sqrt{3}}{2} & \frac{1}{\sqrt{2}} \end{bmatrix}$$
 (10)

Then, to obtain the system stationary model in the dq frame, the Park transformation Equation (11) is employed. This transformation involves converting the variables  $X_{\alpha\beta}$  to  $X_{dq}$ , as defined by:  $X_{dq} = D^T X_{\alpha\beta}$ . Where,

$$D = \begin{bmatrix} \cos \theta & -\sin \theta \\ \sin \theta & \cos \theta \end{bmatrix}, \theta = \tan^{-1} \frac{v_{mg\alpha}}{v_{mg\beta}}.$$
 (11)

in this frame  $v_{mgd} = \sqrt{3} V_{rms}$  and  $v_{mgg} + 0$ .

Now a d-q synchronous frame is employed for the modeling of the AC side, incorporating MG voltages ( $v_{mgd}$ ,  $v_{mgq}$ ) and MG currents ( $i_{mgd}$ ,  $i_{mgq}$ ). The dynamics of capacitors voltages ( $v_{sd}$ ,  $v_{sq}$ ) and inductors currents ( $i_{ld}$ ,  $i_{lq}$ ) are described by equation in (12) (Youssef *et al.*, 2020).

$$\begin{split} \frac{dv_{sd}}{dt} &= wv_{sq} + \frac{1}{2C_f}i_{gd} - \frac{\sqrt{3}}{6C_f}i_{mgq} - \frac{1}{2C_f}i_{sd} + \frac{\sqrt{3}}{6C_f}i_{sq}, \\ \frac{dv_{sq}}{dt} &= -wv_{sd} + \frac{\sqrt{3}}{6C_f}i_{gd} + \frac{1}{2C_f}i_{mgq} - \frac{\sqrt{3}}{6C_f}i_{sd} - \frac{1}{2C_f}i_{sq}, \\ \frac{di_{ld}}{dt} &= wi_{lq} - \frac{1}{2L_f}v_{sd} - \frac{\sqrt{3}}{6L_f}v_{sq} + \frac{1}{2L_f}v_{mgd}, \\ \frac{di_{lq}}{dt} &= wi_{ld} + \frac{\sqrt{3}}{6L_f}v_{sd} - \frac{1}{2L_f}v_{sq} + \frac{1}{L_f}v_{mgq}. \end{split} \tag{12}$$

In this context, w symbolizes the MG angular frequency, while  $L_f$  and  $C_f$  denote the filter inductance and capacitance. Additionally,  $(i_{sd}, i_{sq})$  and  $(i_{mgd}, i_{mgq})$  represent the converter and the grid side currents, respectively.

$$\begin{split} i_{mgd} &= i_{ld} + \left( w \frac{L_f}{R_f} - i_{lq} \right) - \frac{1}{2R_f} v_{sd} - \frac{\sqrt{3}}{6R_f} v_{sq} \\ &\quad + \frac{1}{2R_f} v_{mgd}, \\ i_{mgq} &= i_{lq} + \left( w \frac{L_f}{R_f} - i_{ld} \right) - \frac{1}{2R_f} v_{sq} + \frac{\sqrt{3}}{6R_f} v_{sd} \\ &\quad + \frac{1}{2R_f} v_{mgq}. \end{split} \tag{13}$$

Regarding the injected active P and reactive power Q into the MG, it is determined by the expressions  $P=v_{mgd}\ i_{mgd}-v_{mgq}\ i_{mgq}$  and  $Q=v_{mgq}\ i_{mgd}-v_{mgd}\ i_{mgq}$ , where in this case,  $v_{gq}=0$  within the synchronous reference frame. The currents on the MG side can be derived from equations provided in equation (13). These equations will be instrumental in the design of the MPC-VSG.

From Equation (13) the detailed equation of Q can be calculated from Equation (14):

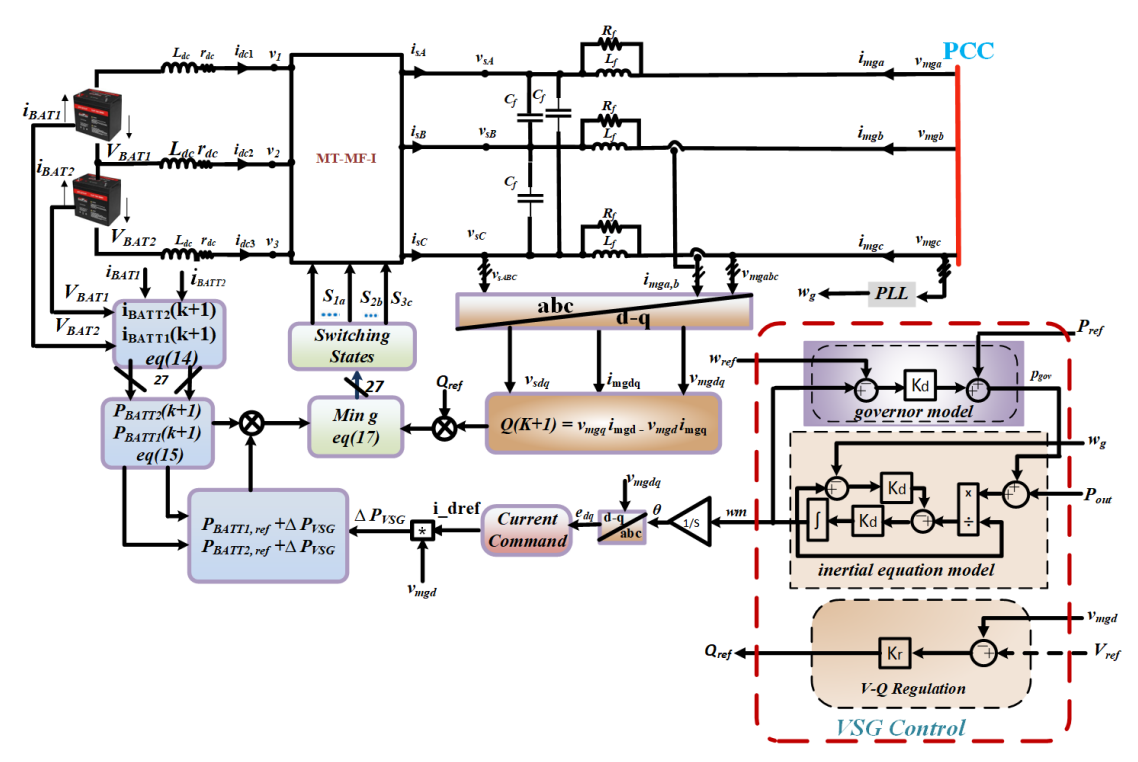


Fig. 4. Proposed VSG based BESS using MPC controller.

$$Q = -v_{mgd}i_{lq} - \frac{\sqrt{3}}{6R_f}v_{mgd}v_{sq} + \frac{1}{2R_f}v_{mgd}v_{sq} + \frac{1}{R_f}v_{mgd}v_{sq} - \left(-\frac{wL_f}{R_f} + w\right)v_{mgd}i_{lq} + v_{mgd}i_{lq} - \frac{1}{2R_f}v_{mgq}v_{sd} - \frac{\sqrt{3}}{6R_f}v_{mgq}v_{sq} + \frac{1}{R_f}v_{mgd}v_{mgq} + \left(\frac{wL_f}{R_f} - w\right)v_{mgd}i_{lq}.$$

$$(14)$$

## 3. Proposed MPC-VSG Based BESS Control Concept

The configuration of the MPC-VSG for the battery management system in the MT-MF inverter is illustrated in Figure 4. It consists of MPC and VSG control components. The MPC component forecasts system variables and calculates the optimal switching states for both sides of the MT-MF inverter. In the VSG control section, command variables for both sides of the inverter, including output voltage command, output current command, and input power command, are established as in (Jongudomkarn *et al.*, 2020); (Babqi 2022).

Variables such as  $V_{BAT1}$ ,  $V_{BAT2}$ ,  $i_{BAT1}$ , and  $i_{BAT2}$  on the DC side are measured to compute the battery power. On the AC side, the line-to-line MG voltages  $V_{mgabc}$  are measured and subsequently transformed into the  $\alpha\beta$  frame to determine the synchronous angle of the MG voltage, denoted as wt. Following this, the MG currents  $i_{mgabc}$ , MG voltages  $V_{mgabc}$ , and the capacitor's voltages  $V_{sabc}$  are converted into d-q coordinates.

#### 3.1. BESS-VSG control design

VSG was introduced to offer inertial support and acts as synchronous generators (SGs) through the BESS. Batteries, the MT-MF inverter, and the output LRC filter can be considered equivalent to the VSG. Figure 4 shows the overall control system configuration, which supports the frequency by simulating the SG swing equation outlined in Equation (15).

$$\begin{split} P_{gov} - P_{out} &= J \frac{dw_m}{dt} + D \big( w_m - w_{ref} \big), \\ P_{out} &= \sum P_{MG} - \sum P_L \\ \frac{d\theta}{dt} &= w_m - w_{PCC}. \end{split} \tag{15}$$

Here,  $P_{out}$  represents the VSG output electrical active power. J and D denote the coefficient of virtual inertia and damping factor, respectively, while  $P_{MG}$  represents generated power,  $P_L$  represents loads power, and  $\theta$  signifies the angle of the rotor position. To simplify, the assumed number of pole pairs for the VSG is one, and  $w_m$  and  $w_{PCC}$  stand for virtual angular speed and angular speed at PCC, respectively.

To emulate the behaviour of an SG, a governor droop control is incorporated as a primary frequency control stage (Ma et al., 2023). This governs the mechanical input power of the VSG according to Equation (16).

$$P_{qov} = P_{ref} + K_d(w_m - w_{PCC}), (16)$$

Here,  $P_{ref}$  is reference power, equivalent to BESS-rated power, and  $K_d$  is the power-frequency control droop coefficient. In the context of the "V- Q droop regulation" principle of the synchronous generator, the reactive power Q is implemented

to oversee the system voltage and can be calculated using Equation (17):

$$Q_{ref} = (V_{ref} - V_{mgd})K_v. (17)$$

Where  $V_{ref}$  and  $V_{mgd}$  denote the reference voltage and grid direct voltage in the dq frame, correspondingly, and  $K_{v}$  is the droop constant.

#### 3.2. Current command

As depicted in Figure 4, the frequency is determined by the "VSG control block," incorporating concepts from the VSG control scheme discussed in the last subsection. The current command " $i_{d_ref}$  generator" block is established by simulating the correlation between an SG's phase voltage and line current, which can be expressed as illustrated in Equation (18).

$$\begin{bmatrix}
i_{d_{r}ef} \\
i_{q_{r}ef}
\end{bmatrix} = Y \left\{ \begin{bmatrix} E_{d} \\ E_{q} \end{bmatrix} - \begin{bmatrix} V_{mgd} \\ V_{mgg} \end{bmatrix} \right\},$$
Where,  $Y = \frac{R_{f} * X_{f}}{R_{f}^{2} + X_{f}^{2}} \begin{bmatrix} \frac{1}{R_{f}} & \frac{1}{X_{f}} \\ \frac{1}{X_{f}} & \frac{1}{R_{f}} \end{bmatrix}$ . (18)

#### 3.3. BESS-MPC design

The design of MPC is centered around achieving optimal control sequences that effectively mitigate frequency deviation and robustly manage BESS output power. This is accomplished by minimizing the quadratic and convex objective function (Saleh *et al.*, 2023); (Sati *et al.*, 2024) . The FCS-MPC employs the system model and real-time system values to calculate the optimal physical switching states of the inverter directly (Rodriguez *et al.*, 2013).

#### 3.3.1. Forecasting of the battery power

Equations (19, 20) illustrate the anticipated currents and powers of the BESS at the time instant (k + 1) within sampling interval  $T_s$ , which can be derived by the discretization of Equations (5, 6) using the Euler-Forward integration method.

$$\begin{split} \frac{i_{BAT1}(k+1) - i_{BAT1}(k)}{T_s} &= -\frac{r_{dc}}{L_{dc}}i_{BAT1}(k+1) + \\ &+ \frac{2V_{BAT1}(k+1) + V_{BAT2}(k+1) - 2V_{12}(k+1) - V_{23}(k+1)}{3L_{dc}} \end{split}$$

$$\begin{split} &\frac{i_{BAT2}(k+1)-i_{BAT2}(k)}{T_s} - \frac{r_{dc}}{L_{dc}}i_{BAT2}(k+1) \\ &+ \frac{V_{BAT1}(k+1) + 2V_{BAT2}(k+1) - V_{12}(k+1) - 2V_{23}(k+1)}{3L_{dc}} \end{split}$$

(19)

$$P_{BAT11}(k+1) = V_{BAT11}(k+1)i_{BAT11}(k+1),$$

$$P_{BAT12}(k+1) = V_{BAT12}(k+1)i_{BAT12}(k+1).$$
(20)

## 3.3.2. BESS injected reactive power prediction

Discretizing the reactive power equation at the sampling time  $T_{\rm s}$  results in Equation (21):

$$Q(k+1) = \frac{3R_f L_f C_f}{3R_f L_f C_f + L_f T_s + R_f T_s^2} i_{lq}(k) v_{mgd}(k)$$

$$+ \frac{\sqrt{3}C_f (L_f + R_f T_s)}{6R_f L_f C_f + 2L_f T_s + 2R_f T_s^2} v_{mgd}(k) v_{sd}(k)$$

$$+ \frac{T_s (L_f + R_f T_s)}{3R_f L_f C_f + L_f T_s + R_f T_s^2} v_{mgd}(k) i_{sq}(k+1)$$

$$- \frac{3C_f (L_f + R_f T_s)}{6R_f L_f C_f + 2L_f T_s + 2R_f T_s^2} v_{mgd}(k) v_{sq}(k). \quad (21)$$

### 3.3.3. Cost function design of MPC-VSG-based BESS

In the case of the MT-MF inverter, the control system is configured to track references for both BESS active and MG reactive power simultaneously. This simultaneous control can be realized by defining a cost function as follows:

$$g = min \left( J_1 \sum_{n=1}^{2} \left( P_{refn} - P_{BATn}(k+1) \right)^2 + J_2 \left( Q_{ref} - Q(k+1) \right)^2 \right).$$
 (22)

Where  $P_{refn} = P_{BATn,ref} + \Delta P_{VSG}$ . The weights for the active power of batteries and MG reactive power are denoted as  $(J_1, J_2)$ , respectively. Twenty-seven distinct voltage vectors are methodically incorporated into the cost function. The goal is to minimize this cost function, determining the associated switch state to be applied in the subsequent cycle.

## 4. Results and discussion

The MG under study serves as a test system to showcase the effectiveness of the proposed MT-MF inverter. This is done to assess how the proposed converter impacts its frequency response. As illustrated in Figure 1, an isolated PV-dieselstorage MG model was developed using MATLAB/SIMULINK software. The simulation involves three sets of simulations as in (Long *et al.*, 2021); (Eid *et al.*, 2022) each set comprises a simulation comparison between:

- The first model is MG normal operation without the existence of BESS.
- The second model is the MPC-based BESS control system.
- The third model is the proposed scheme using MPC-VSG-based BESS using the proposed MF-MT inverter

Before assessing the proposed method's performance under various conditions, it's crucial to select the appropriate inertia and damping coefficients. The impact of different inertia and damping coefficients on a frequency transient is tested. Based on comparing different coefficients for suppressing frequency fluctuations, a set of suitable inertia and damping coefficients is chosen for the proposed method, as outlined in Table 3.

#### 4.1. Case 1: Unexpected load variation

In the normal operation, The PV power generation initially maintains a constant at 500~kW and DG generates 180~kW to supply loads with rating 640~kW as shown in Figures 5(a)

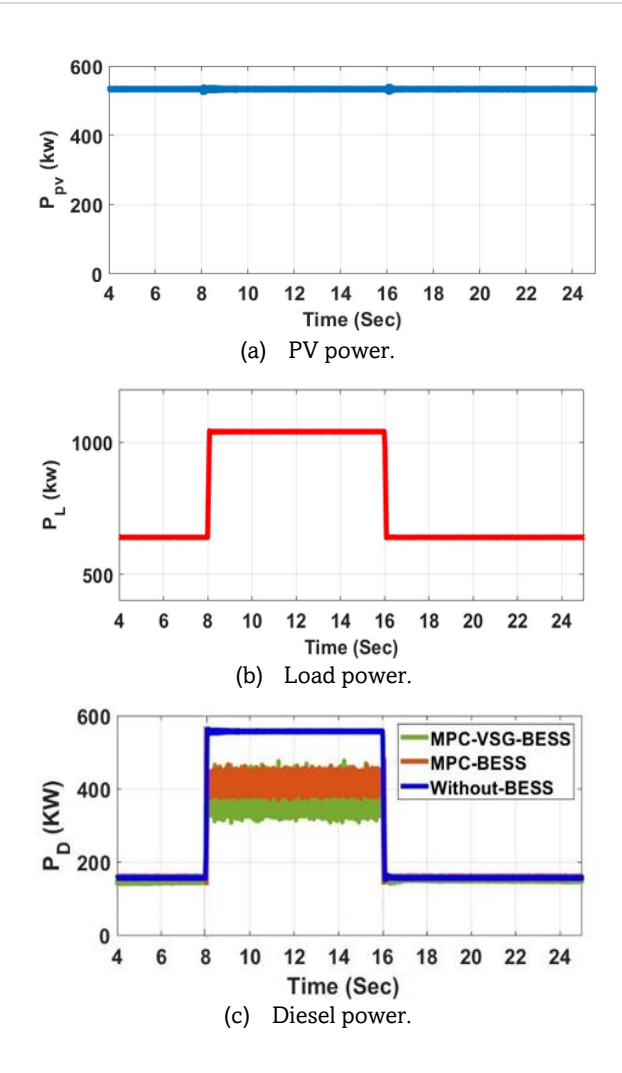
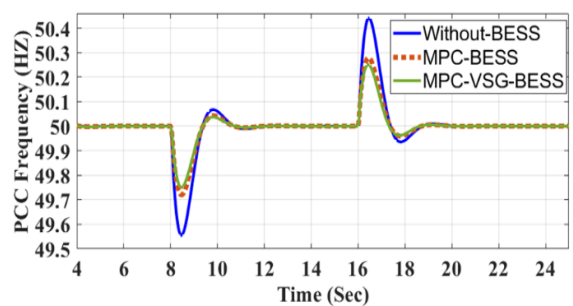


Fig. 5. System dynamic response under load variation.

and 5(b). During unexpected load increasing with 400 KW at 8 seconds (s) and lasts 8 s as shown in Figures 5(c), The conventional generation unit generates the required power, 580 KW, to balance the demand and generated power appears the needed power is within the diesel-rated power range (1 MW). Employing BESS affects the power variation of diesel generators (Babqi 2022). It is evident that as the disturbance magnitude grows, the immediate response of the diesel generator escalates. When confronted with a disturbance of 400 kW, the BESS promptly and effectively responds to mitigate the disturbance, with the diesel generator playing a lesser role (Sati et al., 2024). As the BESS contributions increase, the contributions of the Diesel Generators decrease, as depicted in Figure 5(c). The BESS works as a distributed generator (DG) to support the MG at the disturbance.

Regarding the frequency response during load variation, Figure 6 demonstrates the frequency at PCC in normal operation without BESS and with (MPC-BESS, VSG-BESS). In normal operation, DG inertial response only addresses the power imbalance, the system frequency reaches 49.559, due to insufficient inertia support power and the lack of damping properties to counteract frequency changes. Resulting in a rate of change of frequency (ROCOF) of 0.94 Hz/s, and a restoration time of 4.9421s. However, when BESS is employed, the shortfall in generated power is counteracted by the inherent inertia of the diesel generator, parallel with the energy



**Fig. 6.** System frequency under load transition for different strategies.

stored in the BESS, which supplies fast-change power, smoother power, and aids in stabilizing the frequency during the transient period (Sati *et al.*, 2024). Therefore, employing BESS enhances the frequency response; using MPC-based BESS results in improved frequency nadir and minimized ROCOF, and their values are 49.72Hz and 0.589 Hz/s, respectively. The restoration time is 4.122s (Elwakil *et al.*, 2023). Using MPC-VSG-based BESS gives the best frequency nadir due to the significant increase in the system's inertia and damping capability and stability provided by the VSG. It's important to highlight that the proposed method introduced the shortest restoration time, and the best ROCOF, and their values are 3.877 s and 0.534 Hz/s.

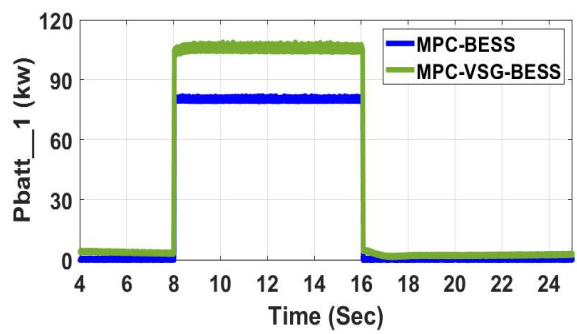
The MT-MF inverter with MPC controller enhances the frequency response in VSG-based BESS mode, in this mode the MPC, and virtual inertia are considered in the controller to design the required power to ensure frequency stability instead of using load power management in case of MPC-BESS mode (Eid *et al.*, 2022). The performance of the MT-MF inverter with MPC-BESS strategy and MPC-VSG-based BESS are evaluated concerning its capacity (as designed in the model) to autonomously regulate and oversee the BESS side while producing the necessary primary power.

Figures 7(a) and 7(b) represent the DC output power from two batteries (Pbatt\_1 and Pbatt\_2) that are connected in the DC side of MT-MF inverter. It can be observed that the main advantage of multi-terminal inverter is to control independently the dc sources to share power depending on the state of charge of battery. In this case, the amount of sharing power of two batteries is almost the same for two modes whereas it has the same state of charge (SOC), as it is designed in the model (Eid *et al.*, 2022).

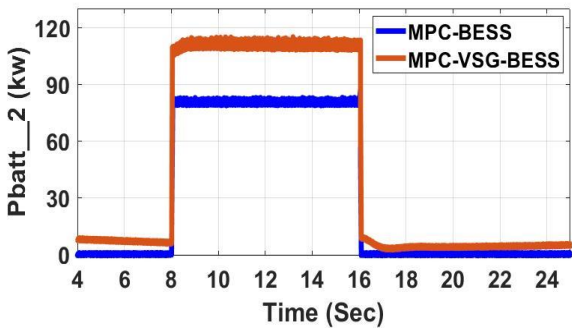
Refereeing to the DC power and reactive power of the MT-MF inverter, it can be noticed from Table 4, that the total power shared from the BESS for MPC-based BESS generates about 160 kw, while the proposed strategy generates about 210 kw during load transitions, as depicted in Figure 7(c), due to the existence of virtual inertia and damping power calculated from MPC controller. On the other side, the AC side of the inverter, the reactive power at the PCC, closely follows the reference as presented in Figure 7(d) (Li *et al.*, 2019).

To conclude the results of this case, Table 4 lists the main parameters to compare the performance of each mode, whereas these modes are normal operation, MPC-BESS, and MPC-VSG-based BESS, as listed in the table. For each mode, the shared power of each unit in the microgrid (PV, diesel, and batteries) is listed, in addition to the nadir frequency, ROCOF, and restoration time. From the obtained results, the performance of the MT-MF inverter in Virtual Synchronous Generator mode using model predictive controller is highly

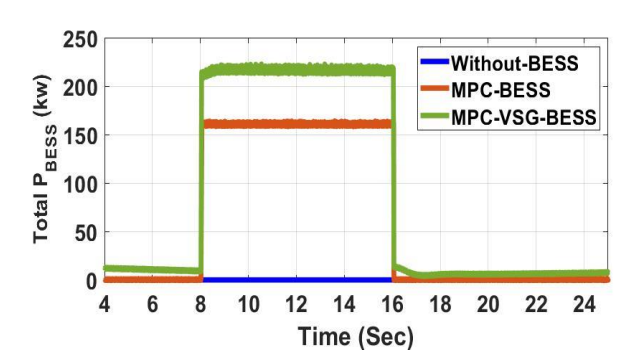
optimized performance and more significant, where it achieves the most favorable Frequency Nadir, minimal ROCOF, quickest restoration time, and significantly distributes power from the batteries to the system.



(a) Power of battery1 of BESS.



(b) Power of battery2 of BESS.



(c) Power gernerated by MT-MF inverter based BESS.

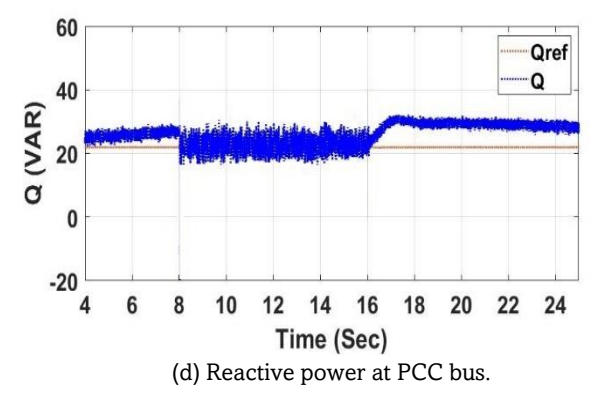


**Fig. 7.** BESS batteries shared power and MG reactive power under load transition.

**Table 4**Summarized obtained results for case 1.

Controllers	Normal Operation	MPC- based- BESS	MPC-VSG- based BESS
Frequency Nadir (Hz)	49.559	49.72	49.7503
ROCOF (Hz/s)	0.9488	0.589	0.534
Restoration Time (s)	4.944	4.122	3.877
P <sub>D</sub> (kW)	580	420	370
P <sub>BESS</sub> (kW)	0	160	210
$P_{batt_{1}}(kW)$	0	80	110
P <sub>batt_2</sub> (kW)	0	80	100

#### 4.2. Case 2: Irradiance change

In this case, the PV is regulated using the MPPT method (Podder, Roy, and Pota 2019), ensuring it provides the maximum power corresponding to the solar irradiance. A sudden decrease in solar irradiance from 1000 to 800 W/m^2 at t=8 s and continues 8 s. Hence, reduces the generated power of the PV from 0.5 MW to 0.3 MW, as depicted in Figures 8(a), the load power remains constant at 640 kW as presented in Figure 8(b).

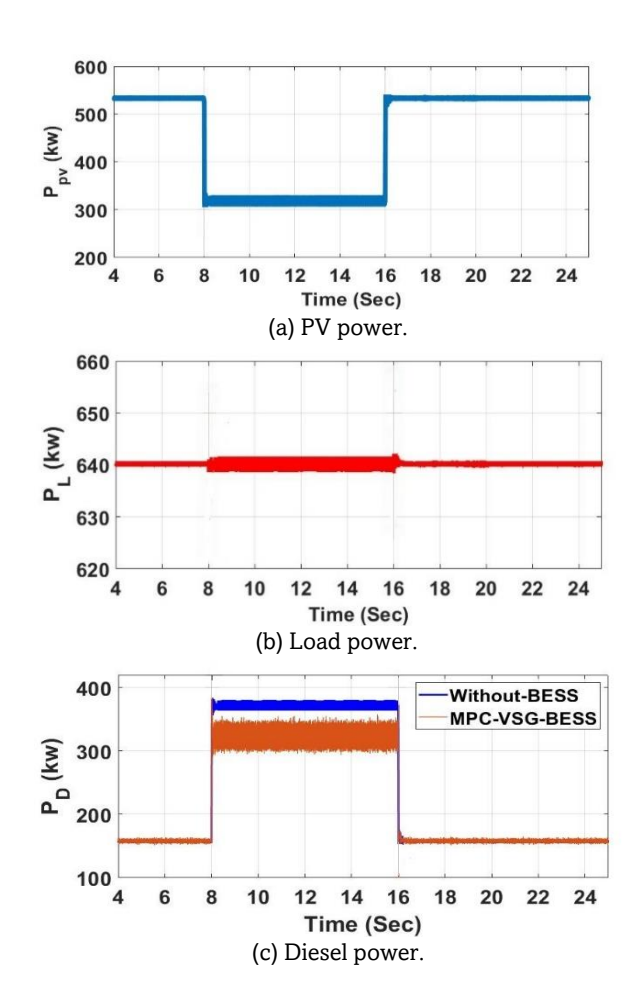
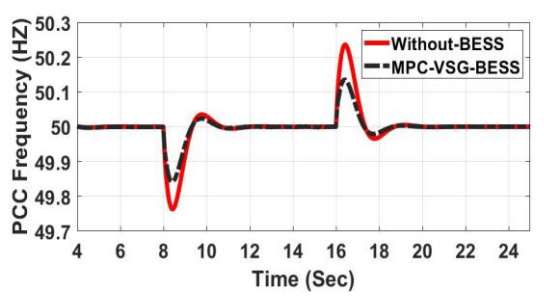


Fig. 8. System dynamic response under irradiance change.



**Fig. 9.** System frequency under irradiance change for different strategies.

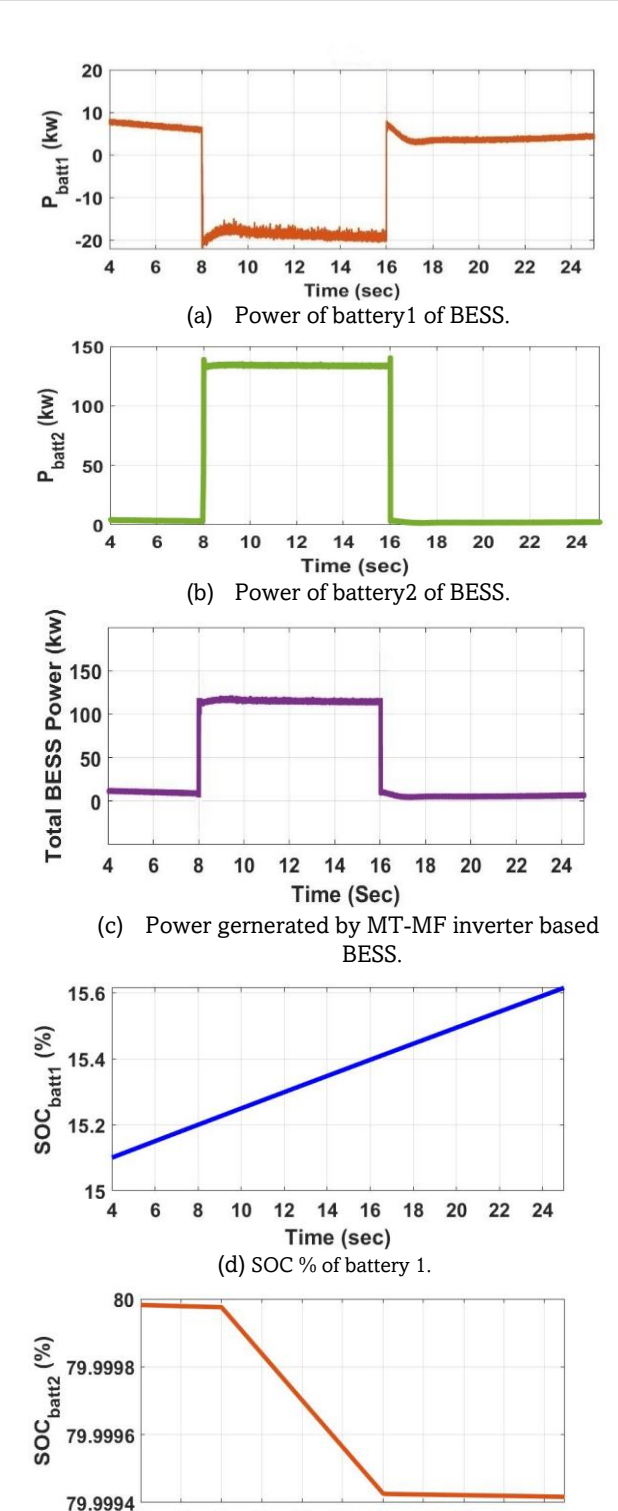
In normal operation, DG generates 180 kW to supply loads as presented in Figure 8 (c). Through the unexpected drop in PV power generation, DG supplies the loads with the required power of 380 kW to equalize the power balance between the demanded and generated power. Employing BESS for the proposed system influences the power variation of diesel generators. As the disturbance magnitude increases, the immediate response of the diesel generator grows rapidly. When PV power generation decreases, the BESS quickly and effectively responds to compensate for the disturbance because of existence of the control methodology of MT-MT inverter, with the diesel generator playing a lesser role.

Figure 9 shows the frequency response during irradiance change at PCC in normal operation and proposed system operation where BESS is employed with the MPC-VSG control. Under normal operation, the DG inertia responses solely due to its low inertia, focuses on rectifying the power imbalance. As a result, the system frequency drops to 49.7669 HZ due to inadequate inertia support power and the absence of damping characteristics to counteract frequency fluctuations (Sati et al., 2024). This results in a ROCOF of 0.6613 Hz/s and a restoration time of 3.9444 s. However, with the introduction of BESS, the loss in generated power is mitigated by the inherent inertia of the diesel generator, along with the energy stored in the BESS, added to the system's inertia and damping power of the virtual generator calculated by the MPC controller, which assists in stabilizing the frequency during the transient period. Consequently, the employment of BESS yields even better frequency nadir, ROCOF, and the shortest restoration time, with values of 49.8544 Hz, 0.5639 Hz/s, and 3.8087 s, respectively (Elwakil et al., 2023).

The effectiveness of the MT-MF inverter within the proposed system is assessed based on its ability to independently manage and supervise the BESS side while supplying the required primary power. Figures 10(a), 10(b), and

**Table 5**Summarized obtained results for case 2

Summarized obtained results for case 2.			
Controllers	Normal Operation	MPC-VSG- based BESS	
Frequency Nadir (Hz)	49.7669	49.8544	
ROCOF (Hz/s)	0.6613	0.5639	
Restoration Time (s)	3.9444	3.8087	
$P_D$ (kW)	380	370	
P <sub>BESS</sub> (kW)	0	110	
$P_{batt_1}(kW)$	0	-20	
$P_{batt_2}(kW)$	0	130	



(e) SOC % of battery 2. **Fig. 10.** BESS batteries shared power and Response of BESS SOC for different charging / discharging battery under irradiance change.

6

12 14 16

Time (sec)

18 20

10(c) represent the DC output power from two batteries ( $P_{\text{batt}\_1}$  and  $P_{\text{batt}\_2}$ ) that are connected in the DC side of MT-MF inverter and total generated power from BESS. It can be observed that the main advantage of multi-terminal inverter is to control independently the dc sources to share power depending on the state of charge (SOC) of battery (Eid *et al.*, 2022); (Youssef *et al.*, 2019). In this case, the first battery

(batt\_1) is operating at charging mode from (0 to -20 kw). While the second (batt\_2) is operating at discharging mode from (0 to 130 kw). Figures 10(c) and (d) present the dynamic response of BESS showing that the SOC as designed in the model in this case is 15% for batt\_1 and 80% for batt\_2.

In summarizing the outcomes of this case, Table 5 provides a comprehensive comparison of key parameters across different operational modes, namely normal operation, and MPC-VSG-based BESS, as detailed in the table. Each mode includes data on the power contributions from various units in the MG (such as PV, diesel, and batteries), along with metrics like nadir frequency, ROCOF, and restoration time. Upon analysis, the results highlight the superior performance of the MT-MF inverter when operating in Virtual Synchronous Generator mode with a model predictive controller. This configuration demonstrates the most favorable frequency nadir, minimal rate of change of frequency, shortest restoration time, and notably efficient distribution of power from the batteries to the system.

#### 4.3. Case 3: Generation contingency events

During this disturbance, the PV, which is producing 0.5 MW, is abruptly disconnected from the MG after 8 s and stays for 8 s, as illustrated in Figure 11(a). Consequently, this results in a severe generation shortage that needs to be handled quickly before excessive frequency deviation is reached (Mohamed *et al.*, 2022). Throughout this period, the load remains constant at 0.64 MW, as shown in Figure 11(b).

During normal operation, the DG immediately adjusts its output power to compensate for the decreased power,

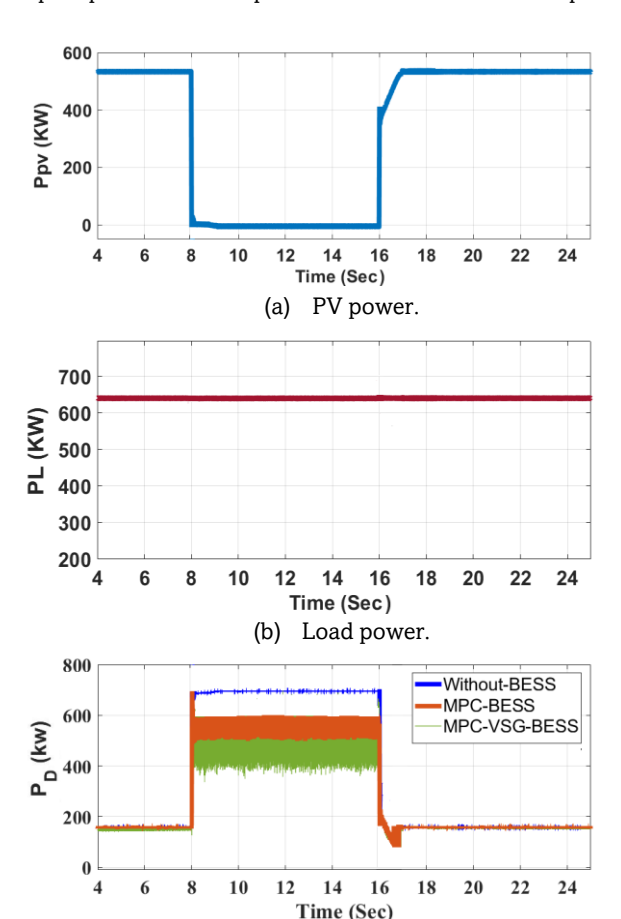


Fig. 11. System dynamic response under load variation.

(c)

Diesel power.

supplying 660 kW to the MG, where it now becomes the only generator unit in the MG. In contrast, for the "MPC-BESS" and "MPC-VSG-based BESS" strategies, the DG and BESS collaborate to supply the required power for the additional load, restoring the power balance, but the DG plays a lesser role due to the used control constrains, where the more aids of BESS the more reductions of the shared power of DG, as shown in Figure 11(c).

Accordingly, in normal operation without BESS, the system shows a severe transient frequency variation. The MG frequency drops below 49.4 Hz, the ROCOF also rises sharply, reaching 1.519 Hz/s, while the restoration time extends to about 4.1692 s, as illustrated in Figure 12. This situation occurs because the diesel generator can only address the power imbalance, lacking sufficient inertia support power and damping properties to mitigate frequency variations (Elwakil *et al.*, 2023).

On the contrary, with implementing of BESS, in the MPC-BESS and MPC-VSG-BESS strategies (Long et al., 2021), the deficit in generated power is offset by both the inherent inertia of the diesel generator and the energy stored in the BESS, thereby aiding in stabilizing the frequency during transient periods. Consequently, the incorporation of BESS enhances the frequency response. When employing MPC-based BESS, there is an improvement in frequency nadir and a reduction in ROCOF, with values of 49.5727 Hz and 1.0369 Hz/s, respectively, and a restoration time of 3.6966 seconds (Mohamed et al., 2022). On the other hand, MPC-VSG-based BESS achieves the best frequency nadir because the MT-MF inverter, coupled with an MPC controller, pumps inertia power calculated from VSG, acquiring a fast response due to the correct compensating signal generated by the MPC. rather than relying on load power management as in the MPC-BESS mode. Notably, this approach introduces the shortest restoration time and the best ROCOF, with values of 3.1769 s and 0.9415 HZ/s, respectively. The MT-MF inverter with MPC-BESS strategy and MPC-VSG-based BESS is assessed regarding its ability to independently regulate and supervise the BESS side while generating the necessary primary power (Eid et al., 2022).

In this case, for (MPC-BESS and MPC-VSG-BESS), the two batteries need to be in discharge mode to compensate for the demanded power, as observed in Figures 13(a) and 13(b). The DC output power from two batteries (Pbatt\_1 and Pbatt\_2) that are connected in the DC side of the MT-MF inverter is controlled independently to share power depending on the state of charge of the battery. In this case, the amount of powersharing between two batteries is almost the same for the two modes, whereas it has the same state of charge (SOC) (Youssef et al., 2019).

As depicted in Figure 13 (c), the MPC-BESS generates lower DC power than the MPC-VSG-BESS during generation

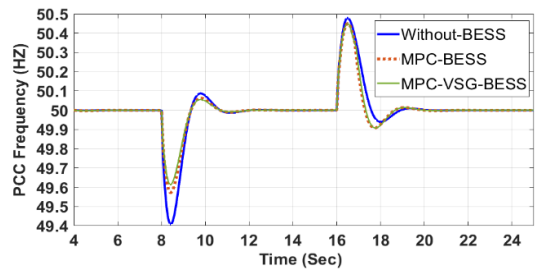


**Fig. 12.** System frequency under load transition for different strategies.

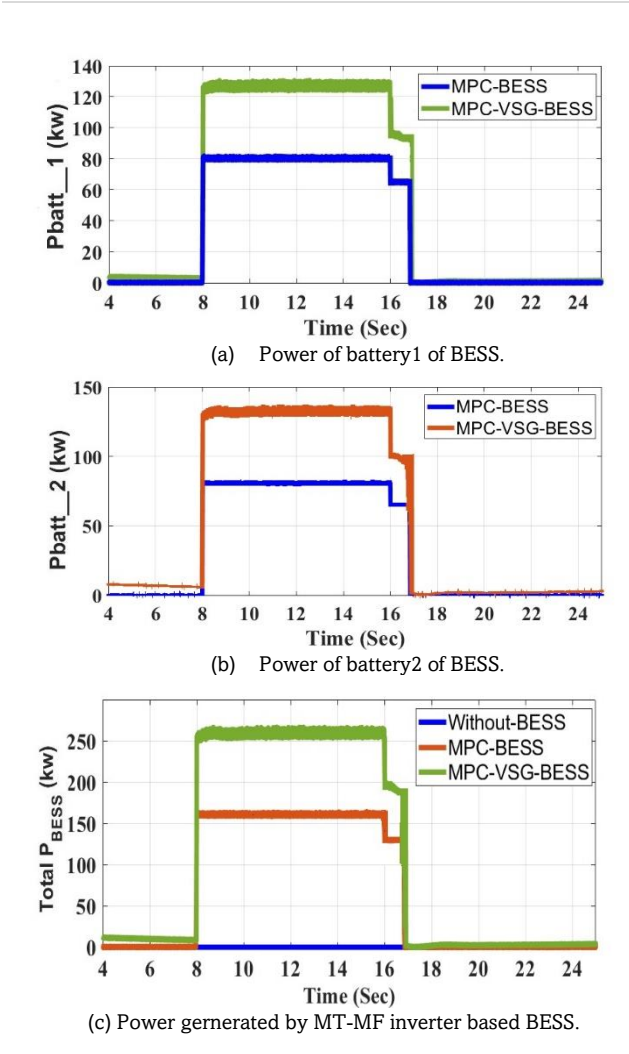


**Fig. 13.** BESS batteries shared power and MG reactive power under load transition.

**Table 6**Summarized obtained results for case 3.

Controllor	Normal	MPC-	MPC- VSG-
Controllers	Operation	based-BESS	based BESS
Frequency Nadir (Hz)	49.4098	49.5727	49.6172
ROCOF (Hz/s)	1.519	1.0369	0.9415
Restoration Time (s)	4.1692	3.6966	3.1769
P <sub>D</sub> (kW)	660	505	405
P <sub>BESS</sub> (kW)	0	155	255
$P_{batt_{1}}(kW)$	0	80	125
P <sub>batt_2</sub> (kW)	0	75	130

loss due to virtual inertia and damping power calculated from the MPC controller added to the MPV-VSG-BESS strategy.

#### 5. Conclusion

This paper proposes a novel MT-MF-based BESS. The battery system was controlled using the MPC-VSG approach. The mathematical model of a VSG is established to predict the optimal output power of VSG to enhance the dynamic

characteristics of system frequency and improve the transient stability of a hybrid MG. In addition, the MT-MF enables the connection of multiple batteries, provides individualized control for each, and allows the BESS to deliver reactive power, improving the BESS-VSG's capacity to manage dynamic reactive power support.

The simulation results validated enhancing frequency stability during disturbances such as load variation, irradiance change, and loss of generation. In addition, validated the independent control for multiple BESS at different operating points for the proposed MT-MF configuration.

Future research will focus on optimizing the control of both DC and AC side systems. Additionally, while the strategy was solely validated and analyzed through simulation models in this study, its performance in real MG environments and under varied experimental parameters still needs to be tested. Further investigations are warranted to refine the strategy's efficacy in practical settings.

Author Contributions: D.E.: Conceptualization, Methodology, Software, Validation, Formal analysis, Investigation, Data curation, writing original draft, Writing – review & editing, Visualization., E.Y.: Conceptualization, Methodology, Validation, Resources, Writing – review & editing., S.E.: Investigation, Writing Review, Editing, Visualization & Supervision., A.E.: Investigation, Writing—Review, Editing, Visualization & Supervision., F.E.: Investigation Writing—Review, Editing, Visualization & Supervision. All authors have read and agreed to the published version of the manuscript.

**Funding:** The authors received no financial support for the research, authorship, and/or publication of this article.

Conflicts of Interest: The authors declare no conflict of interest.

## References

Alberto, B., Alberto, N. C., Mario, P., Gaetano, C., & Aurelio, S. (2011).

Synchronized Phasors Monitoring During the Islanding Maneuver of an Active Distribution Network. *IEEE Transactions on Smart Grid, 2*(1), 82-91. https://doi.org/10.1109/ISGT.2010.5434733.

Alessandro, G., Emanuele, D., & Alessandro, D. (2019). Model Predictive Control of Energy Storage Systems for Power Regulation in Electricity Distribution Networks. 2019 IEEE International Conference on Systems, Man and Cybernetics (SMC), 3365-3370. https://doi.org/10.1109/SMC.2019.8914059.

Babqi, Abdulrahman J. 2022. 'A Novel Model Predictive Control for Stability Improvement of Small Scaled Zero-Inertia Multiple DGs Micro-Grid'. *Periodica Polytechnica Electrical Engineering and Computer Science* 66(2):163–73. https://doi.org/10.3311/PPee.19232

Beck, H.-P., & Hesse, R. (2007, October 9-11). Virtual synchronous machine. 2007 9th International Conference on Electrical Power Quality and Utilisation, 1-7. https://doi.org/10.1109/EPQU.2007.4424220.

Benhamed, S. I. (2016). Dynamic modeling of diesel generator based on electrical and mechanical aspects. 2016 IEEE Electrical Power and Energy Conference (EPEC), (pp. 1-6). https://doi.org/10.1109/EPEC.2016.7771756.

Bø, T. I., & Johansen, T. A. (2017). Battery Power Smoothing Control in a Marine Electric Power Plant Using Nonlinear Model Predictive Contro. *IEEE Transactions on Control Systems Technology*, 25(4), 1449-1456. https://doi.org/10.1109/TCST.2016.2601301

Eid, D., Elmasry, S., El Samahy, A. E., & Youssef, E. (2022, November 7-9). Optimal virtual synchronous generator control of AC/DC matrix converter-based PV grid- connected systems. 13th Mediterranean Conference on Power Generation, Transmission,

- Distribution and Energy Conversion (MEDPOWER 2022, 2022, 88-93. https://doi.org/10.1049/icp.2022.3308.
- Elwakil, M. M., Zoghaby, H. M. El, Sharaf, S. M., & Mosa, M. A. (2023). "Adaptive virtual synchronous generator control using optimized bang-bang for Islanded microgrid stability improvement". Protection and Control of Modern Power Systems, 8(1), 57. https://doi.org/10.1186/s41601-023-00333-7
- Felix, G. T., Carlos, B., & Miguel A., R. (2019). Optimal Economic Schedule for a Network of Microgrids With Hybrid Energy Storage System Using Distributed Model Predictive Contro. {IEEE Transactions on Industrial Electronics, 66(3), 1919-1929. https://doi.org/10.1109/TIE.2018.2826476.
- Gauthier, D., Bruno, F., & Gilles, M. (2012). Dynamic Frequency Control Support by Energy Storage to Reduce the Impact of Wind and Solar Generation on Isolated Power System's Inertia. *IEEE Transactions on Sustainable Energy, 3*(4), 931-939. https://doi.org/10.1109/TSTE.2012.2205025.
- Ghodsi, M. R., Tavakoli, A., & Samanfar, A. (2022). 'Microgrid Stability Improvement Using a Deep Neural Network Controller Based VSG. *International Transactions on Electrical Energy Systems*, 2022(5), 1-17. https://doi.org/10.1155/2022/7539173.
- Hassanzadeh, M. E., Nayeripour, M., Hasanvand, S., & Waffenschmidt, E. (2020). Decentralized control strategy to improve dynamic performance of micro-grid and reduce regional interactions using BESS in the presence of renewable energy resources. *Journal of Energy Storage*, 31, 101520. https://doi.org/10.1016/j.est.2020.101520.
- Hirase, Y., Abe, K., Sugimoto, K., Sakimoto, K., Bevrani, H., & Ise, T. (2018). A novel control approach for virtual synchronous generators to suppress frequency and voltage fluctuations in microgrids. *Applied Energy*, 210, 699-710. https://doi.org/10.1016/j.apenergy.2017.06.058.
- Huijie, C., Zhikang, S., Chao, S., Xuan, L., Zuy, L., & Z. John, S. (2020). Transient Angle Stability of Paralleled Synchronous and Virtual Synchronous Generators in Islanded Microgrids. *IEEE Transactions on Power Electronics*, 35(8), 8751-8765. https://doi.org/10.1109/TPEL.2020.2965152.
- Jongudomkarn, J. (2020). Model Predictive Control for Indirect Boost Matrix Converter Based on Virtual Synchronous Generator. *IEEE Access*, 8, 60364-60381. https://doi:10.1109/ACCESS.2020.2983115
- Kazem, H. A., Albadi, M. H., Al-Waeli, A. H., Al-Busaidi, A. H., & Chaichan, M. T. (2017). Techno-economic feasibility analysis of 1MW photovoltaic grid connected system in Oman. Case Studies in Thermal Engineering, 10, 131-141. https://doi.org/10.1016/j.csite.2017.05.008.
- Kerdphol, T., Rahman, F. S., Watanabe, M., & Mitani, Y. (2020). Virtual Inertia Synthesis and Control. Springer International Publishing. Retrieved February 18, 2024
- Khooban, M. H., Niknam, T., Blaabjerg, F., & Dragicevic, T. (2017). A new load frequency control strategy for micro-grids with considering electrical vehicles. *Electric Power Systems Research*, 143, 585-598. https://doi.org/10.1016/j.epsr.2016.10.057.
- Li, Y., Li, G., Li, Q., Jin, N., Hu, S., Guo, L., & Liu, J. (2019). Model Predictive Control of Grid-connected Converter Based on Virtual Synchronous Machine. 2019 IEEE 8th International Conference on Advanced Power System Automation and Protection (APAP), 1294–1298. https://doi.org/10.1109/APAP47170.2019.9224930
- Linbin, H., Huanhai, X., Zhen, W., Kuayu, W., Haijiao, W., Jiabing, H., & Cencen, L. (2017). A Virtual Synchronous Control for Voltage-Source Converters Utilizing Dynamics of DC-Link Capacitor to Realize Self-Synchronization. *IEEE Journal of Emerging and Selected Topics in Power Electronics*, 5(4), 1565-1577. https://doi.org/10.1109/JESTPE.2017.2740424.
- Liu, J., Miura, Y., & Ise, T. (2016). Comparison of Dynamic Characteristics Between Virtual Synchronous Generator and Droop Control in Inverter-Based Distributed Generators. *IEEE Transactions on Power Electronics*, 31(5), 3600-3611. https://doi.org/10.1109/TPEL.2015.2465852.
- Long, Bo, Yong Liao, Kil To Chong, Jose Rodriguez, and Josep M. Guerrero. 2021. 'MPC-Controlled Virtual Synchronous

- Generator to Enhance Frequency and Voltage Dynamic Performance in Islanded Microgrids'. IEEE Transactions on Smart Grid 12(2):953–64. https://doi.org/10.1109/TSG.2020.3027051
- Rosewater, D. M., Copp, D. A., Nguyen, T. A., Byrne, R. H., & Santoso, S. (2019). Battery Energy Storage Models for Optimal Control. IEEE Access, 7, 178357–178391. https://doi.org/10.1109/ACCESS.2019.2957698.
- Ma C, S. J. (2023). Transient Stability Enhancement Strategy for Islanded Microgrids Based on Energy Storage-Virtual Synchronous Machine Control. *Energies*, 16(17), 6390. https://doi.org/10.3390/en16176390
- Mostafa, F., A., C. C., W., S.-P. J., Ehsan, N., Lingling, F., A., M.-A. P., . . . Jim, R. (2020). Microgrid Stability Definitions, Analysis, and Examples. *IEEE Transactions on Power Systems*, 35(1), 13-29. https://doi.org/10.1109/TPWRS.2019.2925703.
- Mukund R. Patel, Omid Beik. (1999). *Wind and solar energy*. CRC Press. LLC. https://doi.org/10.1201/9781003042952.
- Mohamed, M. M., El Zoghby, H. M., Sharaf, S. M., & Mosa, M. A. (2022). Optimal virtual synchronous generator control of battery/supercapacitor hybrid energy storage system for frequency response enhancement of photovoltaic/diesel microgrid. *Journal of Energy Storage*, 51, 104317. https://doi.org/10.1016/j.est.2022.104317
- Oulcaid, M., El Fadil, H., Yahya, A., & Giri, F. (2016). Maximum Power Point Tracking Algorithm for Photovoltaic Systems under Partial Shaded Conditions. *IFAC-PapersOnLine*, 49(13), 217-222. https://doi.org/10.1016/j.ifacol.2016.07.954.
- Podder, A. K., Roy, N. K., & Pota, H. R. (2019). MPPT methods for solar PV systems: a critical review based on tracking nature. IET Renewable Power Generation, 13(10), 1615–1632. https://doi.org/10.1049/iet-rpg.2018.5946
- Pratap, A., Ziadi, Z., Urasaki, N., & Senjyu, T. (2015). Smoothing of Wind Power Fluctuations for Permanent Magnet Synchronous Generator-Based Wind Energy Conversion System and Fault Ride-through Consideration. *Electric Power Components and Systems*, 43(3), 271-281. https://doi.org/10.1080/15325008.2014.983620.
- Rodriguez, J. a.-R. (2019). State of the Art of Finite Control Set Model Predictive Control in Power Electronics. *IEEE Transactions on Industrial Informatics*, 9(2), 1003-1016. https://doi.org/10.1109/TII.2012.2221469.
- Rodríguez, P., Citro, C., Candela, J., Rocabert, J., & Luna, A. (2018). Flexible Grid Connection and Islanding of SPC-Based PV Power Converters. *IEEE Transactions on Industry Applications*, 24(3), 2690-2702. https://doi.org/10.1109/TIA.2018.2800683.
- Saleh A, H. H. (2023). Optimal Model Predictive Control for Virtual Inertia Control of Autonomous Microgrids. Sustainability, 15(6), 5009. https://doi.org/10.3390/su15065009
- Sati, S. E., Al-Durra, A., Zeineldin, H., EL-Fouly, T. H. M., & El-Saadany, E. F. (2024). A novel virtual inertia-based damping stabilizer for frequency control enhancement for islanded microgrid. International Journal of Electrical Power & Energy Systems, 155, 109580. https://doi.org/10.1016/j.ijepes.2023.109580
- Sikder, P. S., & Pal, N. (2020). Modeling of an intelligent battery controller for standalone solar-wind hybrid distributed generation system. *Journal of King Saud University Engineering Sciences*, 32(6), 368–377. https://doi.org/10.1016/j.jksues.2019.02.002
- Stadler, M., & Naslé, A. (2019). Planning and implementation of bankable microgrids. *The Electricity Journal*, *32*(5), 24-29. https://doi.org/10.1016/j.tej.2019.05.004.
- Tremblay O, D. L.-A. (2009). Experimental Validation of a Battery Dynamic Model for EV Applications. *World Electric Vehicle Journal*, 3(2), 289-298. doi: https://doi.org/10.3390/wevj3020289
- Ur Rehman, H., Yan, X., Abdelbaky, M. A., Jan, M. U., & Iqbal, S. (2021). An advanced virtual synchronous generator control technique for frequency regulation of grid-connected PV system. International Journal of Electrical Power & Energy Systems, 125, 106440. https://doi.org/10.1016/j.ijepes.2020.106440.
- Yousef, M. Y., Mosa, M. A., Ali, A. .., & El Masry, S. M. (2021). Frequency response enhancement of an AC micro-grid has

- renewable energy resources based generators using inertia controller. *Electric Power Systems Research*, *196*, 107194. https://doi.org/10.1016/j.epsr.2021.107194.
- Youssef E, C. P. (2020). Direct Power Control of a Single Stage Current Source Inverter Grid-Tied PV System. *Energies*, 13(12), 3165. doi:https://doi.org/10.3390/en13123165.
- Youssef, E., Pinto, S. F., Amin, A., & El Samahy, A. E. (2019). Multi-Terminal Matrix Converters as Enablers for Compact Battery Management Systems. *IECON 2019 - 45th Annual Conference of* the *IEEE Industrial Electronics Society*, 1, 1874-1879. https://doi.org/10.1109/IECON.2019.8926823.
- Zhang, X., Gao, Q., Guo, Z., Zhang, H., Li, M., & Li, F. (2020).

  Coordinated control strategy for a PV-storage grid-connected system based on a virtual synchronous generator. *Global Energy Interconnection*, 3(1), 51-59. https://doi.org/10.1016/j.gloei.2020.03.003.
- Zhikang, S., Chao, S., Xuan, L., Zuyi, L., & Z. John, S. (2019). Transient Angle Stability of Virtual Synchronous Generators Using Lyapunov's Direct Method. *IEEE Transactions on Smart Grid*, 10(4), 4648-4661. https://doi.org/10.1109/TSG.2018.2866122.
- Zhong, C., Li, H., Zhou, Y., Lv, Y., Chen, J., & Li, Y. (2022). Virtual synchronous generator of PV generation without energy storage for frequency support in autonomous microgrid. *International Journal of Electrical Power & amp; Energy Systems, 134*, 107343. Retrieved from https://doi.org/10.1016%2Fj.ijepes.2021.107343
- Zhong, Q.-C., & Weiss, G. (2011). Synchronverters: Inverters That Mimic Synchronous Generators. *IEEE Transactions on Industrial Electronics*, 58(4), 1259-1267. https://doi.org/10.1109/TIE.2010.2048839.



© 2024. The Author(s). This article is an open access article distributed under the terms and conditions of the Creative Commons Attribution-ShareAlike 4.0 (CC BY-SA) International License (http://creativecommons.org/licenses/by-sa/4.0/)